



Fermi surface transformation at the pseudogap critical point of a cuprate superconductor

Yawen Fang^{1,10}, Gaël Grissonnanche^{1,2,3,10}, Anaëlle Legros^{1,3,4}, Simon Verret³, Francis Laliberté³, Clément Collignon³, Amirreza Ataei³, Maxime Dion³, Jianshi Zhou⁵, David Graf⁶, Michael J. Lawler^{1,7}, Paul A. Goddard⁸, Louis Taillefer^{3,9} and B. J. Ramshaw^{1,9} ✉

The nature of the pseudogap phase remains a major puzzle in our understanding of cuprate high-temperature superconductivity. Whether or not this metallic phase is defined by any of the reported broken symmetries, the topology of its Fermi surface remains a fundamental open question. Here we use angle-dependent magnetoresistance (ADMR) to measure the Fermi surface of the $\text{La}_{1.6-x}\text{Nd}_{0.4}\text{Sr}_x\text{CuO}_4$ cuprate. Outside the pseudogap phase, we fit the ADMR data and extract a Fermi surface geometry that is in excellent agreement with angle-resolved photoemission data. Within the pseudogap phase, the ADMR is qualitatively different, revealing a transformation of the Fermi surface. We can rule out changes in the quasiparticle lifetime as the sole cause of this transformation. We find that our data are most consistent with a pseudogap Fermi surface that consists of small, nodal hole pockets, thereby accounting for the drop in carrier density across the pseudogap transition found in several cuprates.

A long-standing mystery of high- T_c cuprate superconductors is the ‘pseudogap phase’—a correlated electronic state whose key characteristic is a loss of coherent quasiparticles below onset temperature T^* and below critical doping p^* . This loss of quasiparticles is reminiscent of the superconducting gap that opens at transition temperature T_c (hence the name ‘pseudogap’), suggesting that the pseudogap phase and superconductivity are related. Characterizing what remains of the coherent Fermi surface (FS) inside the pseudogap phase is, therefore, a critical step towards understanding how this peculiar metallic state gives rise to, or is compatible with, high-temperature superconductivity.

Heavily overdoped cuprates are good metals with a well-defined FS. $\text{Tl}_2\text{Ba}_2\text{CuO}_{6+\delta}$ (Tl-2201) has been extensively measured in this doping regime, and three independent experiments agree on the geometry of the FS, namely, angle-dependent magnetoresistance (ADMR)², angle-resolved photoemission spectroscopy (ARPES)³ and quantum oscillations⁴. Other cuprates, such as $\text{La}_{2-x}\text{Sr}_x\text{CuO}_4$ and $\text{Bi}_2\text{Sr}_2\text{CaCu}_2\text{O}_{8+\delta}$, show similar agreement between the measured FS and band structure calculations for $p > p^*$ (ref. 5). As the doping is lowered towards p^* , the FS measured by ARPES remains well defined but the electrical resistivity becomes progressively more anomalous, becoming perfectly linear in temperature at p^* (refs. 6,7). Whether a T -linear scattering rate alone can account for this anomalous resistivity has been the subject of much debate: we have addressed this topic in a recent study⁸.

Cuprates enter the pseudogap phase below p^* . Although this phase is also metallic, its FS—in the limit $T \rightarrow 0$ and in the absence of superconductivity—remains unknown. ARPES measurements performed above T_c and below T^* find discontinuous segments known as Fermi arcs⁵, which defy the conventional definition of a closed FS. Quantum oscillations, on the other hand, reveal a small, closed,

electron-like FS (electron pocket)⁹. This pocket, however, appears only in the presence of the charge density wave (CDW) order¹⁰, and the CDW order is not always observed over the same range of dopings as the pseudogap phase itself. For example, although the CDW order extends up to p^* in $\text{HgBa}_2\text{CuO}_{4+x}$ (ref. 11), it terminates before p^* at $p \approx 0.16$ in $\text{YBa}_2\text{Cu}_3\text{O}_{6+x}$ (ref. 12) and at $p \approx 0.18$ in $\text{La}_{1.6-x}\text{Nd}_{0.4}\text{Sr}_x\text{CuO}_4$ (ref. 13) (Nd-LSCO, the compound studied here). The spin density wave (SDW) order has also been found below p^* in several cuprates^{14–16}. Recent neutron diffraction measurements have even found indications of the SDW order in Nd-LSCO at $p = 0.24$, in a zero magnetic field, and at $T = 13$ K (ref. 15) (Fig. 1). Although the SDW order is known to reconstruct part of the FS at much lower doping¹⁷, our sample at $p = 0.24$ shows perfectly linear resistivity down to 2 K at $B = 35$ T, without an upturn at $T = 13$ K that would be a characteristic of the SDW order¹⁸ (Extended Data Fig. 1). This suggests that either there are differences between the samples grown by different groups or that a magnetic field suppresses the SDW order at $p = 0.24$.

A crucial question, therefore, remains: what is the FS of cuprates immediately below p^* in the absence of superconductivity or CDW order? There are two possibilities: (1) the FS is the same above and below p^* , but the quasiparticles become incoherent below p^* due to scattering or other correlation effects; (2) the FS below p^* is different from the FS above p^* . Demonstration of the latter scenario would imply that either the translational symmetry is broken (on some appropriate length scale) in the pseudogap phase or it is a phase with a topological order¹⁹.

Experiment

To investigate the possibility of FS reconstruction below p^* , we turn to the cuprate $\text{La}_{1.6-x}\text{Nd}_{0.4}\text{Sr}_x\text{CuO}_4$. The critical doping $p^* = 0.23$ that

¹Laboratory of Atomic and Solid State Physics, Cornell University, Ithaca, NY, USA. ²Kavli Institute at Cornell for Nanoscale Science, Ithaca, NY, USA.

³Département de physique, Institut quantique, and RQMP, Université de Sherbrooke, Sherbrooke, Québec, Canada. ⁴SPEC, CEA, CNRS-UMR 3680, Université Paris-Saclay, Gif-sur-Yvette, France. ⁵Materials Science and Engineering Program, Department of Mechanical Engineering, University of Texas at Austin, Austin, TX, USA. ⁶National High Magnetic Field Laboratory, Tallahassee, FL, USA. ⁷Department of Physics, Applied Physics and Astronomy, Binghamton University, Binghamton, NY, USA. ⁸Department of Physics, University of Warwick, Coventry, UK. ⁹Canadian Institute for Advanced Research, Toronto, Ontario, Canada. ¹⁰These authors contributed equally: Yawen Fang, Gaël Grissonnanche. ✉e-mail: bradramshaw@cornell.edu

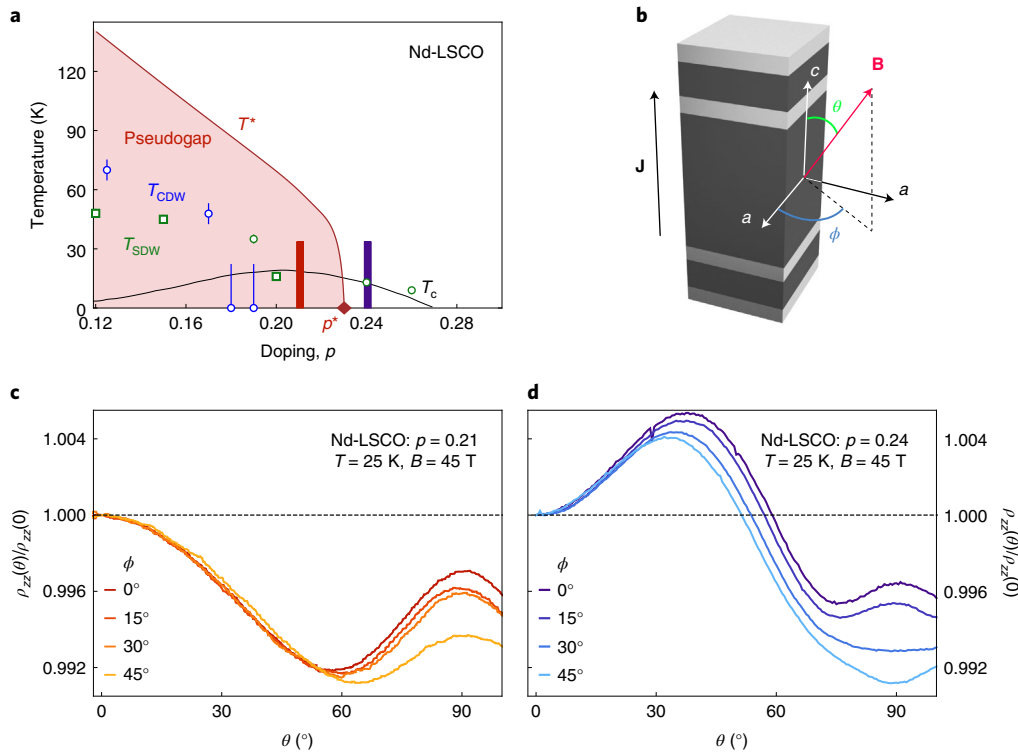


Fig. 1 | ADMR above and below the pseudogap critical doping p^* in Nd-LSCO. **a**, Temperature–doping phase diagram of the hole-doped cuprate Nd-LSCO in zero magnetic field. The pseudogap phase is highlighted in red (onset temperature T^* is taken from the resistivity^{7,20} and ARPES²² measurements). The critical doping where the pseudogap phase ends is $p^* = 0.23$ (red diamond²⁰). The superconducting dome is marked by a solid black line and can be entirely suppressed with $\mathbf{B} \parallel c \geq 20$ T. The onset of a short-range CDW order, as detected by resonant X-ray scattering¹³, is indicated by the blue circles. The onset of an SDW order, as detected by neutron scattering, is indicated with green circles¹⁵ and green squares⁵⁸. The red and blue bars correspond to the dopings and temperature ranges measured in this study. **b**, Geometry of the ADMR measurements. The sample is represented in grey with silver contacts. The black arrow identifies the direction of electric current \mathbf{J} along the c axis. The angles ϕ and θ indicate the direction of magnetic field \mathbf{B} with respect to the crystallographic a and c axes. **c**, Angle-dependent c -axis resistivity $\rho_{zz}(\theta)$ of Nd-LSCO at $p = 0.21$ ($< p^*$). All the data are taken at $T = 25$ K and $B = 45$ T as a function of θ for $\phi = 0^\circ, 15^\circ, 30^\circ$ and 45° , and normalized by the $\theta = 0$ value, $\rho_{zz}(0)$. **d**, Data taken under the same conditions as **c**, but for Nd-LSCO at $p = 0.24$ ($> p^*$). Note that certain features change substantially across p^* , including the peak near $\theta = 40^\circ$ and the ϕ dependence near $\theta = 90^\circ$.

marks the onset of the pseudogap phase in Nd-LSCO has been well characterized by transport^{7,20}, specific heat²¹ and ARPES²² measurements. At $p = 0.20$, a gap opens along the ‘anti-nodal’ directions of the Brillouin zone ($\phi = 0^\circ, 90^\circ, 180^\circ$ and 270°) on cooling below $T^* = 75$ K, followed by an upturn in the resistivity; at $p = 0.24$, ARPES detects no anti-nodal gap and the resistivity remains perfectly linear down to the lowest measured temperature. Note that the highest doping where X-ray scattering detects the CDW order in Nd-LSCO is $p = 0.17$ (ref. 13). As with other cuprates^{23,24}, the onset of the CDW order in Nd-LSCO coincides with a downturn in the Hall coefficient towards negative values²⁵. At $p \geq 0.20$, the Hall coefficient remains positive at all the temperatures and magnetic fields²⁰. This suggests that the quasiparticles responsible for transport (and hence, ADMR) do not feel the influence of any remnant CDW order at the dopings where we perform our measurements, in agreement with the absence of any CDW modulations detected by X-ray diffraction and the Seebeck coefficient at $p \geq 0.18$ (refs. 13,26).

To determine whether the FS is transformed across p^* , we measure variations in the c -axis resistivity ρ_{zz} of Nd-LSCO at $p = 0.21$ and $p = 0.24$ as a function of the polar (θ) and azimuthal (ϕ) angles between the sample and external magnetic field \mathbf{B} (Fig. 1b–d)—a technique known as ADMR. These variations are determined by the three-dimensional (3D) geometry of the FS and the momentum dependence of the scattering rate. The basic premise of ADMR is that the velocities of charge-carrying quasiparticles are modified by the Lorentz force in a magnetic field. Within the standard

relaxation-time approximation, ρ_{zz} is given by the Chambers’ solution to the Boltzmann transport equation:

$$1/\rho_{zz} = \frac{e^2}{4\pi^3} \oint d^2\mathbf{k} \mathcal{D}(\mathbf{k}) v_z[\mathbf{k}(t=0)] \int_{-\infty}^0 v_z[\mathbf{k}(t)] e^{t/\tau} dt \quad (1)$$

where $\oint d^2\mathbf{k}$ is an integral over the FS, $\mathcal{D}(\mathbf{k})$ is the density of states at point \mathbf{k} , v_z is the component of the Fermi velocity in the z direction and $\int_{-\infty}^0 v_z[\mathbf{k}(t)] e^{t/\tau} dt$ is an integral of v_z weighted by the probability that a quasiparticle with lifetime τ scatters after time t (ref. 27). The magnetic field \mathbf{B} enters through the Lorentz force $\hbar \frac{d\mathbf{k}}{dt} = e\mathbf{v} \times \mathbf{B}$, where \hbar is the reduced Planck constant and e is the elementary charge, which induces the quasiparticles into cyclotron motion around the FS (Fig. 2c).

For a quasi-two-dimensional FS with simple, sinusoidal warping, ρ_{zz} can be analytically calculated using equation (1) in the limit where τ is long²⁸. The exact calculation contains special Yamaji angles where all the cyclotron orbits have the same cross-sectional area perpendicular to the magnetic field and where the v_z component of the Fermi velocity averages to zero around each orbit. This cancellation of v_z results in the maxima in the c -axis resistivity at these angles. The Yamaji angles are determined by the geometry of the FS; therefore, by measuring the angular positions of the resistivity maxima, one can construct the FS geometry. For more complex FS geometries, equation (1) must be numerically calculated, but the intuition still holds—at certain angles, the resistivity

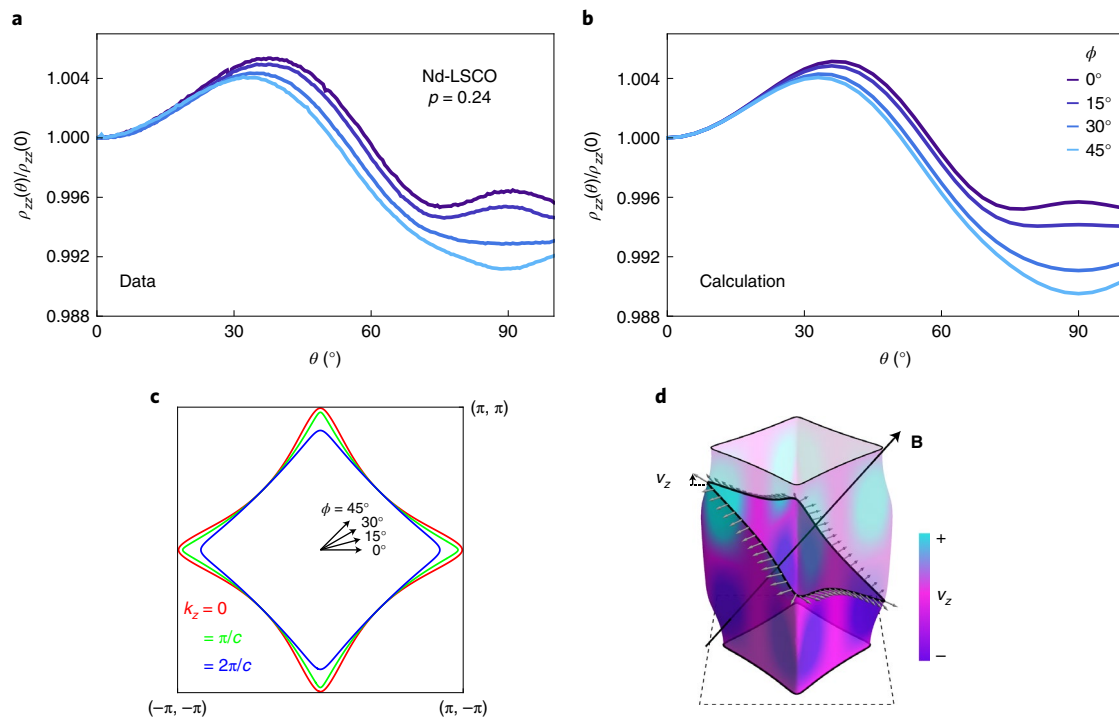


Fig. 2 | ADMR and FS of Nd-LSCO at $p = 0.24$. **a**, The ADMR of Nd-LSCO at $p = 0.24$ as a function of θ at $T = 25$ K and $B = 45$ T. **b**, Simulations obtained from Chambers' formula using the tight-binding parameters from Extended Data Table 2 and the scattering rate model from equation (4). **c**, The FS of Nd-LSCO at $p = 0.24$ obtained from the ADMR calculations, with cuts shown at $k_z = 0$, π/c , and $2\pi/c$, where c is the height of the body-centred tetragonal unit cell (and $c/2$ is the distance between the copper oxide layers). **d**, The full 3D FS. The colouring corresponds to the v_z component of the Fermi velocity, with positive v_z in light blue, negative v_z in purple and $v_z = 0$ in magenta. A single cyclotron orbit, perpendicular to the magnetic field, is drawn in black, with the Fermi velocity at different points around the orbit indicated with grey arrows. The strong variation in v_z around the cyclotron orbit is what leads to ADMR.

is maximized because v_z is more effectively averaged towards zero (Supplementary Fig. 1).

To reconstruct the FS geometry from the ADMR data, we start with a tight-binding model $\epsilon(\mathbf{k})$ that respects the geometry of the transfer integrals of the material, define the Fermi velocity as $\mathbf{v} = \frac{1}{\hbar} \nabla_{\mathbf{k}} \epsilon$, and then tune the tight-binding parameters until the calculated ρ_{zz} matches the measured data. In addition to the FS geometry, ADMR is sensitive to the momentum dependence of quasiparticle scattering. This is captured in equation (1) by introducing $\tau(\mathbf{k})$ —the full expression for ρ_{zz} in this case is given in Methods. We separate the scattering rate into isotropic and anisotropic components, that is, $1/\tau(\mathbf{k}) = 1/\tau_{\text{iso}} + 1/\tau_{\text{aniso}}(\mathbf{k})$. These two components can have distinct temperature dependencies, as demonstrated for TI-2201 (ref. 29). The approach of using equation (1) to determine FSs has been particularly successful in two-dimensional (2D) metals such as organic conductors³⁰ and Sr_2RuO_4 (ref. 31). In cuprates, ADMR has been measured in the overdoped regime ($p > p^*$)^{2,8}, in the underdoped regime with the CDW order ($p \approx 0.1 \ll p^*$)³² and in electron-doped materials³³, but never in the pseudogap phase in the absence of the CDW order.

Doping above p^*

Figure 1d shows the ADMR of Nd-LSCO at $p = 0.24$, at $T = 25$ K and $B = 45$ T. We fit the data using a single-band tight-binding model that is commonly used for cuprates with a body-centred tetragonal unit cell (Methods provides the full model). We then perform a global optimization over the tight-binding and scattering rate parameters using a genetic algorithm, placing loose bounds on the parameters around values determined by previous ARPES measurements^{22,34}. Figure 2b (right) shows the results of this optimization: the key features reproduced by the fit include the position

of the maximum near $\theta = 40^\circ$, the onset of ϕ dependence beyond $\theta = 40^\circ$ and the ϕ -dependent peak/dip near $\theta = 90^\circ$. The best-fit tight-binding parameters are in good agreement with those determined by ARPES (Extended Data Table 1), demonstrating excellent consistency between the two techniques.

The peak in ρ_{zz} near $\theta = 40^\circ$, which is captured well by the fit, can also be checked against the intuitive picture of ADMR described earlier: the position of this peak should be related to the length of the Fermi wavevector k_F . For an FS with the simplest sinusoidal dispersion along k_z , an analytical calculation of equation (1) shows that the ADMR changes with the angle as $\rho_{zz} \propto 1/(J_0(ck_F \tan \theta))^2$, where c is the interlayer lattice constant, k_F is the Fermi wavevector and J_0 is the zeroth Bessel function of the first kind. Although the analytical expression for ρ_{zz} is not exact for the particular form of interlayer hopping found in Nd-LSCO, Supplementary Fig. 1 shows that the maxima in resistivity coincide with the angles where v_z is best averaged to zero. Our analysis including proper interlayer hopping shows that the peak in ρ_{zz} near $\theta = 40^\circ$ suggests that $k_F \approx 7 \text{ nm}^{-1}$ along the zone diagonal, which is very close to the FS shown in Fig. 2c. This suggests that the ADMR at $p = 0.24$ exhibits features consistent with a large, unreconstructed FS, as also observed by ARPES.

In addition to the FS geometry, ADMR is sensitive to the momentum-dependent quasiparticle scattering rate. We find that the data for $p = 0.24$ are best described by a highly anisotropic scattering rate that is the largest near the anti-nodal regions of the Brillouin zone and the smallest near the nodal regions. More details of the scattering rate model and its temperature dependence are provided elsewhere⁸.

Doping below p^*

We now turn to Nd-LSCO at $p = 0.21$, below p^* and inside the pseudogap phase, where ARPES finds discontinuous segments of

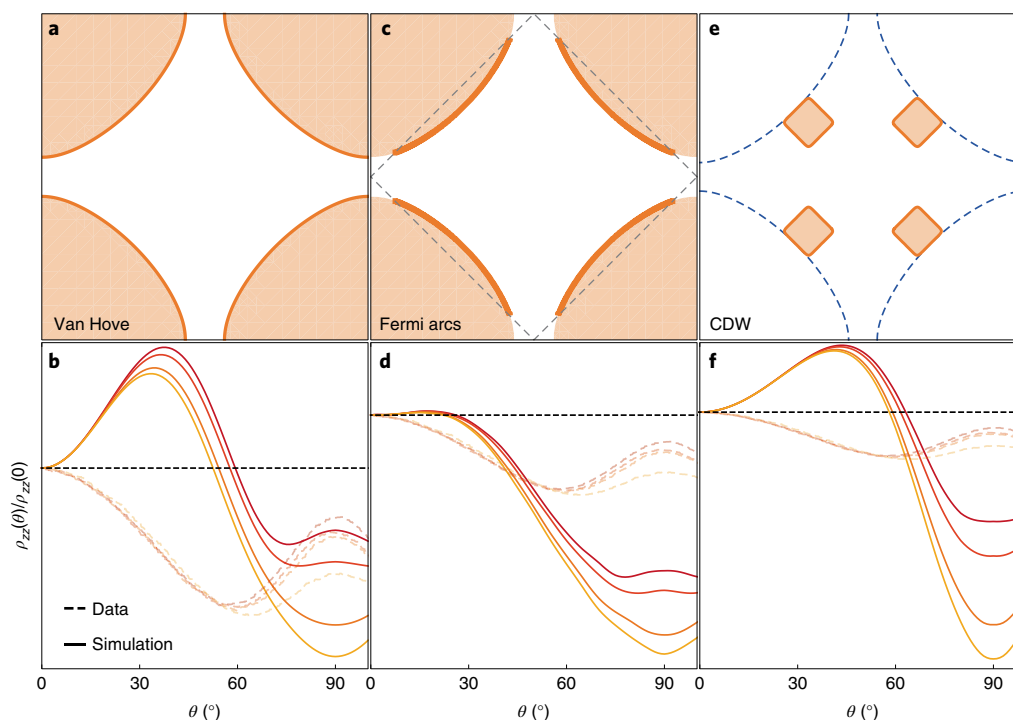


Fig. 3 | Models that fail to account for the change in ADMR across p^* . **a–f**, The FS for three different scenarios (**a,c,e**) and the resulting ADMR simulations (**b,d,f**). **b**, ADMR calculated using the same parameters as in Fig. 2a (including the scattering rate) but with the chemical potential shifted past the Van Hove singularity to $p=0.21$. The ADMR for this model is largely unchanged from the fit at $p=0.24$. **c**, Schematic of Fermi arcs, where the FS terminates at the antiferromagnetic zone boundary (grey dashed line) due to incoherence of the quasiparticles past that point. This is modelled as a scattering rate that considerably increases on crossing the zone boundary. This model, shown in **d**, fails to fit the data, particularly near $\theta=90^\circ$. **e**, Electron pockets obtained from a period-three CDW order are shown in orange, along with the original FS shown as a blue dashed line. The ADMR calculations for these electron pockets are shown in **f** but do not reproduce the data. Similar nodal electron pockets are able to account for the ADMR in $\text{YBa}_2\text{Cu}_3\text{O}_{6+x}$ at $p=0.11$ (ref. ³²), where the CDW order is present.

FS known as ‘arcs’³⁵. On comparison of Fig. 1c,d, it is immediately apparent that the structure of the ADMR qualitatively changes on entering the pseudogap phase. In particular, the resistivity peak near $\theta=40^\circ$ has disappeared at $p=0.21$. The qualitative differences in the data arise either from a change in the FS geometry or from a large increase in the scattering rate for the anti-nodal quasiparticles (for example, the generation of Fermi arcs).

We test several different scenarios to understand the change in the ADMR across p^* . These scenarios can be divided into two classes: those that change only the quasiparticle scattering rate and those that reconstruct the FS. First, we use the same FS model and scattering rate that fit the ADMR at $p=0.24$ and simply adjust the chemical potential to decrease the hole concentration to $p=0.21$. The simulated data for this model are shown in Fig. 3a. Instead of describing the data for $p=0.21$, however, this simulation appears close to that for $p=0.24$. This is to be expected: only the FS near the anti-nodal region appreciably changes on lowering the doping, and the ADMR is less sensitive to this region due to its high scattering rate. Therefore, something beyond a simple change in the chemical potential must occur when crossing p^* .

Next, we test three other scattering rate models (on the large, unreconstructed FS): the same model used at $p=0.24$, but now the scattering rate parameters are allowed to vary (Extended Data Fig. 2c); isotropic scattering around the entire FS (Fig. 2b); and a model of ‘Fermi arcs’ where the quasiparticle lifetime rapidly diminishes past the antiferromagnetic zone boundary on the FS (Fig. 3c). Even after performing fits using the genetic algorithm, allowing for a broad range of band structure and scattering rate parameters, none of these scattering rate models on the large unreconstructed

hole-like FS are able to reproduce the ADMR at $p=0.21$ (Methods provides a description of the fits and Extended Data Fig. 2). Note that the average strength of scattering does not seem to change much as the system crosses p^* , since the magnitude of the ADMR, which is essentially governed by the magnitude of $1/\tau$, is roughly the same at $p=0.21$ and $p=0.24$ (Fig. 1). The inability of any of these scattering rate models to fit the ADMR at $p=0.21$ suggests that the FS must be reconstructed into a new, geometrically distinct FS in the pseudogap phase.

To confirm a change in the FS geometry across p^* , we test two models for FS reconstruction. First, we try a small electron pocket at nodal positions in the Brillouin zone (Fig. 3e). This FS is the result of a biaxial CDW, as found in several underdoped cuprates^{35,36}, and is probably the origin of the small electron pocket found in $\text{YBa}_2\text{Cu}_3\text{O}_{6+x}$ and $\text{HgBa}_2\text{CuO}_{4+x}$ (ref. ⁹). This FS accounts well for the ADMR of $\text{YBa}_2\text{Cu}_3\text{O}_{6.6}$ at $p=0.11$, where there is CDW order³². We simulate the ADMR using the method described earlier, now calculating the Fermi velocity and density of states using the reconstructed band structure (Fig. 3f shows the results). Even if one allows the tight-binding and gap parameters to vary, or if one uses a d -wave form factor for the CDW gap³⁷, these simulations do not agree at all with the ADMR for Nd-LSCO at $p=0.21$ (Methods and Extended Data Fig. 3). This suggests that the FS transformation at $p=0.21$ is not due to the same CDW order that produces the nodal electron pocket found in other underdoped cuprates. This is consistent with the Hall and Seebeck coefficients, which remain positive at all the temperatures and magnetic fields in Nd-LSCO at $p=0.21$ (refs. ^{20,38}), whereas negative (or negative-trending) Hall and Seebeck coefficients are a ubiquitous signature of charge order in

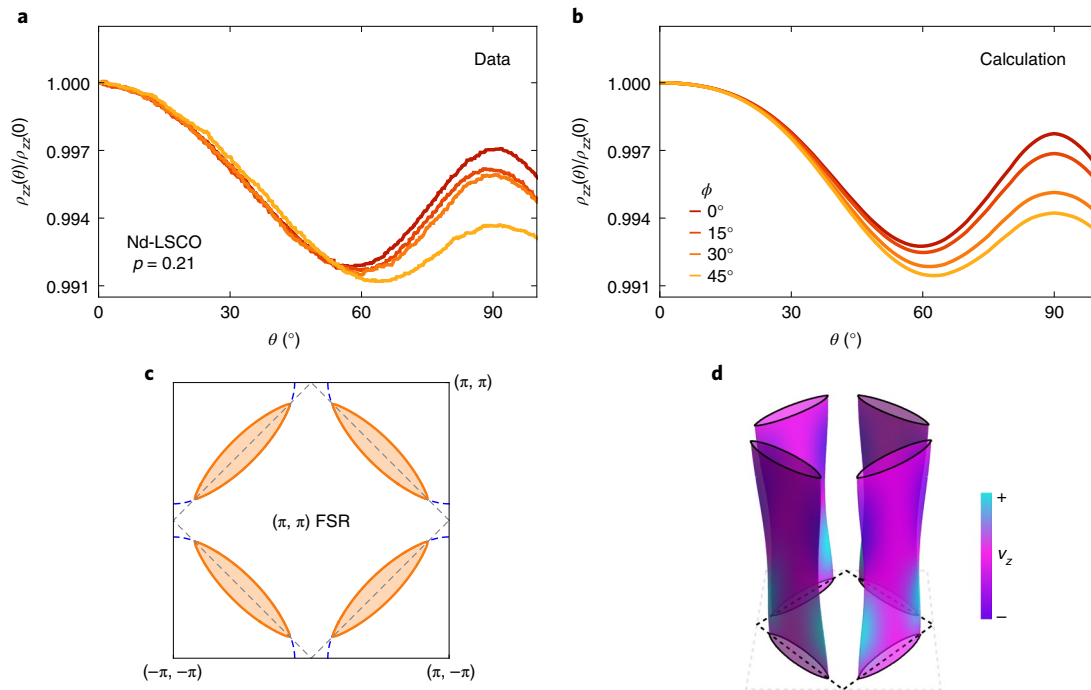


Fig. 4 | FS reconstruction into nodal hole pockets in Nd-LSCO at $p = 0.21$. **a**, Measured ADMR of Nd-LSCO at $p = 0.21$ as a function of θ at $T = 25$ K and $B = 45$ T. **b**, Calculated ADMR for the FS shown in **c** with an isotropic scattering rate. **c**, FS consisting of four nodal hole pockets. These pockets are implemented via a model of antiferromagnetic order with the wavevector $Q = (\pi, \pi)$ and a gap of 55 K, with the electron pockets removed to produce agreement with the measured Hall coefficient. **d**, The full 3D FS at $p = 0.21$ after reconstruction.

cuprates, observed in four distinct families of cuprates^{23,24,39}, including Nd-LSCO at $p = 0.12$ (ref. 25). It is also consistent with recent X-ray scattering experiments, which find no charge order at dopings greater than $x = 0.17$ in Nd-LSCO (ref. 13).

Finally, we consider small hole pockets centred around the nodal directions of the FS (Fig. 4). Such nodal hole pockets arise in various theoretical scenarios^{19,40–43} and the Fermi arcs seen by ARPES could correspond to the front side of such pockets. In practice, we generate an FS made of four nodal hole pockets by reconstructing the large FS using antiferromagnetic order with a $Q = (\pi, \pi)$ wavevector, employing the same tight-binding parameters as in the $p = 0.24$ simulation. The ADMR for this FS is shown in Fig. 4b. This FS reproduces all the critical features of the data at $p = 0.21$: the resistivity initially decreases with increasing θ ; there is a minimum near $\theta = 60^\circ$; and the peak at 90° is the strongest along $\phi = 0^\circ$ and the weakest along $\phi = 45^\circ$. Note that despite the success of this model in reproducing the relative change in magnetoresistance as a function of angle, the absolute value of the resistance is off by approximately a factor of three (Methods).

The key structures present in the reconstructed hole pockets, which are not present in the model of the arcs, are the sharp corners where the front and back sides of the hole pockets are connected: it is these corners that produce qualitatively different ADMR data than those produced by the model of arcs. The gap magnitude (strength of the potential associated with FS reconstruction) that best reproduces the data is 5 meV or ~ 55 K—this gap sets the ‘sharpness’ of the corners on the hole pockets. Note that this gap is insufficient to remove the anti-nodal electron pockets that also result from a $Q = (\pi, \pi)$ reconstruction: we remove the electron pocket to produce agreement between the calculated and measured Hall coefficients (our data are also consistent with the inclusion of electron pockets with a much higher scattering rate than that found for hole pockets; Methods and Extended Data Fig. 4). We find that a momentum-independent scattering rate is required

to reproduce the data. This reduction in scattering rate anisotropy between $p > p^*$ and $p < p^*$ may be due to the substantial reduction in the anisotropy of the density of states when moving from $p = 0.24$ to $p = 0.21$ (Extended Data Fig. 5 shows a reduction in the anisotropy of the density of states from a factor of 25 at $p = 0.24$ to a factor of 2 at $p = 0.21$). Thus, the change in ADMR moving from $p = 0.24$ to $p = 0.21$ has two sources: a transformation to an FS consisting of four nodal hole pockets and a reduction in the scattering rate anisotropy.

Discussion

Our main finding is a qualitative change in ADMR that indicates a transformation of the FS at p^* . For $p > p^*$, excellent agreement is found between the FS measured by ADMR and the one measured by ARPES, both giving the same large, diamond-like FS⁸. For $p < p^*$, however, the ADMR is strikingly different. This difference is not due to a simple lowering of the chemical potential through the Van Hove point nor is it solely due to a change in the scattering rate across p^* : it must, therefore, be due to a change in the geometry of the FS. The data below p^* are best described by an FS composed of nodal hole pockets. These nodal hole pockets can result from a $Q = (\pi, \pi)$ reconstruction. Such a reconstruction is consistent with the transition from the carrier density $n = 1 + p$ at $p > p^*$ to $n = p$ at $p < p^*$, as revealed by the Hall coefficient^{20,44} (Extended Data Fig. 4 shows a comparison of the measured and calculated Hall coefficients). Similar nodal hole pockets were recently detected by both quantum oscillations and ARPES in the five-layer cuprate $\text{Ba}_2\text{Ca}_1\text{Cu}_5\text{O}_{10}(\text{F}_2\text{O})_2$ at a doping level where long-range antiferromagnetic order is known to exist¹⁷; the question is whether a similar reconstruction takes place in Nd-LSCO at $p = 0.21$, given that the SDW correlations at this doping are short ranged and quasistatic^{14,15}.

Many proposals that break translational symmetry in the same way as long-range antiferromagnetism—with a wavevector of $Q = (\pi, \pi)$ —have been put forward, including d -density wave order⁴¹,

staggered loop-current order⁴⁵ and, of course, local-moment antiferromagnetism or SDW order^{43,46}. There are also proposals that produce nodal hole pockets without breaking translational symmetry, including the Yang–Zhang–Rice ansatz⁴², staggered fluxes⁴⁰ and topological order¹⁹. In Supplementary Fig. 2, we show that the nodal hole pockets from the Yang–Zhang–Rice ansatz also fit the ADMR data at $p=0.21$. This suggests that the nodal hole pockets themselves, rather than the particular details of any one model, are what is important to describe the FS transformation across p^* .

Even if no static, long-range order is present in Nd-LSCO at $p=0.21$, scattering at the antiferromagnetic wavevector is known to be important to many models of the pseudogap^{47–49}, and it may be enough for an order parameter to appear static on time scales of the order of the quasiparticle lifetime (approximately 0.1 ps) and over length scales of the order of the cyclotron radius (approximately 20 nm at $B=45\text{ T}$)⁵⁰. We note that there is evidence for fluctuating, short-range SDW correlations in Nd-LSCO near p^* (refs. ^{14,15}), and a short-range magnetic order has been found to onset below p^* in the related compound, namely, $\text{La}_{2-x}\text{Sr}_x\text{CuO}_4$ (ref. ¹⁶). It may be that some form of this SDW reconstructs the FS at $p=0.21$. Note, however, that a reduction in the Hall coefficient within the pseudogap phase is universal in cuprates^{20,51–53}, and that our model of FS transformation produces the correct Hall coefficient (both above and below p^*), which strongly suggests that the model proposed here for the FS below p^* itself is universal, whereas the tendency towards SDW order substantially varies between different cuprates.

Three families of unconventional superconductors—iron pnictides, organics and heavy fermions—share a common phase diagram in which long-range magnetic order is suppressed as a function of doping or pressure. At the critical point, where long-range order is suppressed, the superconducting T_c is typically maximal, resistivity is the most anomalous (typically linear in temperature) and the quasiparticle mass is enhanced^{10,54,55}. Long-range magnetic order reconstructs the FS in all three classes of materials^{54,56,57}, and thus, the onset of FS transformation, near-optimal T_c , T -linear resistivity and enhanced quasiparticle interactions are tied together across dozens of superconducting materials, each with entirely different microscopic constituents. The phase diagram of high- T_c cuprates is superficially similar, with T -linear resistivity, near-optimal T_c and enhanced effective mass occurring at a critical doping where the pseudogap phase appears. What was missing until now was direct experimental evidence of the accompanying FS transformation.

Online content

Any methods, additional references, Nature Research reporting summaries, source data, extended data, supplementary information, acknowledgements, peer review information; details of author contributions and competing interests; and statements of data and code availability are available at <https://doi.org/10.1038/s41567-022-01514-1>.

Received: 13 November 2021; Accepted: 17 January 2022;

Published online: 10 March 2022

References

- Keimer, B., Kivelson, S. A., Norman, M. R., Uchida, S. & Zaanen, J. From quantum matter to high-temperature superconductivity in copper oxides. *Nature* **518**, 179–186 (2015).
- Hussey, N. E., Abdel-Jawad, M., Carrington, A., Mackenzie, A. P. & Balicas, L. A coherent three-dimensional Fermi surface in a high-transition-temperature superconductor. *Nature* **425**, 814–817 (2003).
- Platé, M. et al. Fermi surface and quasiparticle excitations of overdoped $\text{Ti}_2\text{Ba}_2\text{CuO}_{6+\delta}$. *Phys. Rev. Lett.* **95**, 077001 (2005).
- Vignolle, B. et al. Quantum oscillations in an overdoped high- T_c superconductor. *Nature* **455**, 952–955 (2008).
- Damascelli, A., Hussain, Z. & Shen, Z.-X. Angle-resolved photoemission studies of the cuprate superconductors. *Rev. Mod. Phys.* **75**, 473–541 (2003).

- Cooper, R. A. et al. Anomalous criticality in the electrical resistivity of $\text{La}_{2-x}\text{Sr}_x\text{CuO}_4$. *Science* **323**, 603–607 (2009).
- Daou, R. et al. Linear temperature dependence of resistivity and change in the Fermi surface at the pseudogap critical point of a high- T_c superconductor. *Nat. Phys.* **5**, 31–34 (2009).
- Grissonnanche, G. et al. Linear-in temperature resistivity from an isotropic Planckian scattering rate. *Nature* **595**, 667–672 (2021).
- Doiron-Leyraud, N. et al. Quantum oscillations and the Fermi surface in an underdoped high- T_c superconductor. *Nature* **447**, 565–568 (2007).
- Ramshaw, B. J. et al. Quasiparticle mass enhancement approaching optimal doping in a high- T_c superconductor. *Science* **348**, 317–320 (2015).
- Chan, M. K. et al. Extent of Fermi-surface reconstruction in the high-temperature superconductor $\text{HgBa}_2\text{CuO}_{4+\delta}$. *Proc. Natl Acad. Sci. USA* **117**, 9782–9786 (2020).
- Blanco-Canosa, S. et al. Resonant X-ray scattering study of charge-density wave correlations in $\text{YBa}_2\text{Cu}_3\text{O}_{6+x}$. *Phys. Rev. B* **90**, 054513 (2014).
- Gupta, N. K. et al. Vanishing nematic order beyond the pseudogap phase in overdoped cuprate superconductors. *Proc. Natl Acad. Sci. USA* **118**, e2106881118 (2021).
- Tranquada, J. M. et al. Coexistence of, and competition between, superconductivity and charge-stripe order in $\text{La}_{1.6-x}\text{Nd}_{0.4}\text{Sr}_x\text{CuO}_4$. *Phys. Rev. Lett.* **78**, 338–341 (1997).
- Ma, Q. et al. Parallel spin stripes and their coexistence with superconducting ground states at optimal and high doping in $\text{La}_{1.6-x}\text{Nd}_{0.4}\text{Sr}_x\text{CuO}_4$. *Phys. Rev. Research* **3**, 023151 (2021).
- Frachet, M. et al. Hidden magnetism at the pseudogap critical point of a cuprate superconductor. *Nat. Phys.* **16**, 1064–1068 (2020).
- Kunisada, S. et al. Observation of small Fermi pockets protected by clean CuO_2 sheets of a high- T_c superconductor. *Science* **369**, 833–838 (2020).
- Bourgeois-Hope, P. et al. Link between magnetism and resistivity upturn in cuprates: a thermal conductivity study of $\text{La}_{2-x}\text{Sr}_x\text{CuO}_4$. Preprint at <https://arxiv.org/abs/1910.08126> (2019).
- Scheurer, M. S. et al. Topological order in the pseudogap metal. *Proc. Natl Acad. Sci. USA* **115**, E3665–E3672 (2018).
- Collignon, C. et al. Fermi-surface transformation across the pseudogap critical point of the cuprate superconductor $\text{La}_{1.6-x}\text{Nd}_{0.4}\text{Sr}_x\text{CuO}_4$. *Phys. Rev. B* **95**, 224517 (2017).
- Michon, B. et al. Thermodynamic signatures of quantum criticality in cuprate superconductors. *Nature* **567**, 218–222 (2019).
- Matt, C. E. et al. Electron scattering, charge order, and pseudogap physics in $\text{La}_{1.6-x}\text{Nd}_{0.4}\text{Sr}_x\text{CuO}_4$: an angle-resolved photoemission spectroscopy study. *Phys. Rev. B* **92**, 134524 (2015).
- Adachi, T., Noji, T. & Koike, Y. Crystal growth, transport properties, and crystal structure of the single-crystal $\text{La}_{2-x}\text{Ba}_x\text{CuO}_4$ ($x=0.11$). *Phys. Rev. B* **64**, 144524 (2001).
- LeBoeuf, D. et al. Electron pockets in the Fermi surface of hole-doped high- T_c superconductors. *Nature* **450**, 533–536 (2007).
- Noda, T., Eisaki, H. & Uchida, S.-I. Evidence for one-dimensional charge transport in $\text{La}_{2-x}\text{Nd}_x\text{Sr}_x\text{CuO}_4$. *Science* **286**, 265–268 (1999).
- Michon, B. et al. Wiedemann-Franz law and abrupt change in conductivity across the pseudogap critical point of a cuprate superconductor. *Phys. Rev. X* **8**, 041010 (2018).
- Chambers, R. G. The kinetic formulation of conduction problems. *Proc. Phys. Soc. A* **65**, 458–459 (1952).
- Yamaji, K. On the angle dependence of the magnetoresistance in quasi-two-dimensional organic superconductors. *J. Phys. Soc. Jpn* **58**, 1520–1523 (1989).
- Abdel-Jawad, M. et al. Anisotropic scattering and anomalous normal-state transport in a high-temperature superconductor. *Nat. Phys.* **2**, 821–825 (2006).
- Singleton, J. Studies of quasi-two-dimensional organic conductors based on BEDT-TTF using high magnetic fields. *Rep. Prog. Phys.* **63**, 1111–1207 (2000).
- Bergemann, C., Mackenzie, A. P., Julian, S. R., Forsythe, D. & Ohmichi, E. Quasi-two-dimensional Fermi liquid properties of the unconventional superconductor Sr_2RuO_4 . *Adv. Phys.* **52**, 639–725 (2003).
- Ramshaw, B. J. et al. Broken rotational symmetry on the Fermi surface of a high- T_c superconductor. *npj Quantum Mater.* **2**, 8 (2017).
- Kartsovnik, M. V. et al. Fermi surface of the electron-doped cuprate superconductor $\text{Nd}_{2-x}\text{Ce}_x\text{CuO}_4$ probed by high-field magnetotransport. *New J. Phys.* **13**, 015001 (2011).
- Horio, M. et al. Three-dimensional Fermi surface of overdoped La-based cuprates. *Phys. Rev. Lett.* **121**, 077004 (2018).
- Vershinin, M. et al. Local ordering in the pseudogap state of the high- T_c superconductor $\text{Bi}_2\text{Sr}_2\text{CaCu}_2\text{O}_{8+\delta}$. *Science* **303**, 1995–1998 (2004).
- Wu, T. et al. Magnetic-field-induced charge-stripe order in the high-temperature superconductor $\text{YBa}_2\text{Cu}_3\text{O}_7$. *Nature* **477**, 191–194 (2011).
- Allais, A., Chowdhury, D. & Sachdev, S. Connecting high-field quantum oscillations to zero-field electron spectral functions in the underdoped cuprates. *Nat. Commun.* **5**, 5771 (2014).

38. Collignon, C. et al. Thermopower across the phase diagram of the cuprate $\text{La}_{1-x}\text{Nd}_x\text{Sr}_2\text{CuO}_4$: signatures of the pseudogap and charge density wave phases. *Phys. Rev. B* **103**, 155102 (2021).
39. Doiron-Leyraud, N. et al. Hall, Seebeck, and Nernst coefficients of underdoped $\text{HgBa}_2\text{CuO}_{4+\delta}$: Fermi-surface reconstruction in an archetypal cuprate superconductor. *Phys. Rev. X* **3**, 021019 (2013).
40. Wen, X.-G. & Lee, P. A. Theory of underdoped cuprates. *Phys. Rev. Lett.* **76**, 503–506 (1996).
41. Chakravarty, S., Laughlin, R. B., Morr, D. K. & Nayak, C. Hidden order in the cuprates. *Phys. Rev. B* **63**, 094503 (2001).
42. Rice, T. M., Yang, K.-Y. & Zhang, F.-C. A phenomenological theory of the anomalous pseudogap phase in underdoped cuprates. *Rep. Prog. Phys.* **75**, 016502 (2011).
43. Storey, J. G. Hall effect and Fermi surface reconstruction via electron pockets in the high- T_c cuprates. *Europhys. Lett.* **113**, 27003 (2016).
44. Badoux, S. et al. Change of carrier density at the pseudogap critical point of a cuprate superconductor. *Nature* **531**, 210–214 (2016).
45. Li, Z.-X. and Lee, D.-H. The thermal Hall conductance of two doped symmetry-breaking topological insulators. Preprint at <https://arxiv.org/abs/1905.04248> (2019).
46. Lewin, S. K. & Analytis, J. G. Angle-dependent magnetoresistance oscillations of cuprate superconductors in a model with Fermi surface reconstruction and magnetic breakdown. *Phys. Rev. B* **92**, 195130 (2015).
47. S en echal, D. & Tremblay, A.-M. S. Hot spots and pseudogaps for hole- and electron-doped high-temperature superconductors. *Phys. Rev. Lett.* **92**, 126401 (2004).
48. Scalapino, D. J. A common thread: the pairing interaction for unconventional superconductors. *Rev. Mod. Phys.* **84**, 1383–1417 (2012).
49. Wu, W., Ferrero, M., Georges, A. & Kozik, E. Controlling Feynman diagrammatic expansions: physical nature of the pseudogap in the two-dimensional Hubbard model. *Phys. Rev. B* **96**, 041105 (2017).
50. Gannot, Y., Ramshaw, B. J. & Kivelson, S. A. Fermi surface reconstruction by a charge density wave with finite correlation length. *Phys. Rev. B* **100**, 045128 (2019).
51. Badoux, S. et al. Critical doping for the onset of Fermi-surface reconstruction by charge-density-wave order in the cuprate superconductor $\text{La}_{2-x}\text{Sr}_x\text{CuO}_4$. *Phys. Rev. X* **6**, 021004 (2016).
52. Putzke, C. et al. Reduced Hall carrier density in the overdoped strange metal regime of cuprate superconductors. *Nat. Phys.* **17**, 826–831 (2021).
53. Lizaire, M. et al. Transport signatures of the pseudogap critical point in the cuprate superconductor $\text{Bi}_2\text{Sr}_{2-x}\text{La}_x\text{CuO}_{6+\delta}$. *Phys. Rev. B* **104**, 014515 (2021).
54. Shishido, H., Settai, R., Harima, H. & Onuki, Y. A drastic change of the Fermi surface at a critical pressure in CeRhIn_5 : dHvA study under pressure. *J. Phys. Soc. Jpn* **74**, 1103–1106 (2005).
55. Walmsley, P. et al. Quasiparticle mass enhancement close to the quantum critical point in $\text{BaFe}_2(\text{As}_{1-x}\text{P}_x)_2$. *Phys. Rev. Lett.* **110**, 257002 (2013).
56. Uji, S. et al. Rapid oscillation and Fermi-surface reconstruction due to spin-density-wave formation in the organic conductor $(\text{TMTSF})_2\text{PF}_6$. *Phys. Rev. B* **55**, 12446 (1997).
57. Analytis, J. G. et al. Quantum oscillations in the parent pnictide BaFe_2As_2 : itinerant electrons in the reconstructed state. *Phys. Rev. B* **80**, 064507 (2009).
58. Tranquada, J. M., Sternlieb, B. J., Axe, J. D., Nakamura, Y. & Uchida, S. Evidence for stripe correlations of spins and holes in copper oxide superconductors. *Nature* **375**, 561–563 (1995).

Publisher's note Springer Nature remains neutral with regard to jurisdictional claims in published maps and institutional affiliations.

  The Author(s), under exclusive licence to Springer Nature Limited 2022

Methods

Samples and transport measurements. Single crystals of $\text{La}_{2-x}\text{Nd}_x\text{Sr}_y\text{CuO}_4$ (Nd-LSCO) were grown at the University of Texas at Austin using the travelling-float-zone technique, with Nd content of $y=0.4$ and nominal Sr concentrations of $x=0.20, 0.21$ and 0.25 . The hole concentration p is given by $p=x$, with an error of ± 0.003 , except for the $x=0.25$ sample for which $p=0.240 \pm 0.005$ (more details are provided elsewhere²⁰). The value of T_c , defined as the point of zero resistance, is $T_c = 15.5, 15.0$ and 11.0 K for samples with $p=0.20, 0.21$ and 0.24 , respectively. The pseudogap critical point in Nd-LSCO is at $p^* = 0.23$ (ref. 20).

Resistivity measurements were performed in the 45 T hybrid magnet at the National High Magnetic Field Lab. The sample resistance was measured with a standard four-point contact geometry using a Stanford Research Systems 830 lock-in amplifier. The samples were driven with current $I_{\text{rms}} = 1$ mA from a Keithley 6221 current source. The temperature was stabilized to within ± 1 mK around the target temperature at each angle. Uncertainty of the absolute temperature due to thermometer magnetoresistance is negligible at $T=25$ K. The thermometer was mounted at a fixed point on the probe near the sample but not on the rotating platform. Thus, the magnetoresistance of the thermometer did not change as the sample was rotated.

At $p=0.21$ and 0.24 , the upper critical fields of Nd-LSCO are 15 and 10 T, respectively, for $\mathbf{B} \parallel c$ (ref. 21). By applying a magnetic field of $B=45$ T at $T=25$ K, both samples remain in the normal state as the field is rotated from $\mathbf{B} \parallel c$ to $\mathbf{B} \parallel a$.

The polar angle θ between the crystalline c axis and the magnetic field was continuously changed in situ from around -15° to -110° using a single-axis rotator. A voltage proportional to the angle was recorded with each angle sweep. The angle θ was calibrated by finding symmetric points in the resistivity and scaling the measured voltage such that the symmetric points lie at $\theta=0^\circ$ and 90° (Extended Data Fig. 6). This procedure resulted in an uncertainty of $\pm 0.5^\circ$ in θ . The azimuthal angle ϕ was changed by placing the sample on top of G-10 wedges machined at different angles, namely, $15^\circ, 30^\circ$ and 45° . An illustration of the sample mounted on the rotator stage, with a G-10 wedge to set the azimuthal angle to be 30° , is shown in Extended Data Fig. 6. The samples and wedges were aligned under a microscope by eye to an accuracy of $\pm 2^\circ$ in ϕ .

Transport calculations in a magnetic field. The semiclassical electrical conductivity of a metal can be calculated by solving the Boltzmann transport equation within the relaxation-time approximation. The approach most suitable for calculating the angle-dependent magnetoresistance was formulated by Chambers²⁷. It provides an intuitive prescription for calculating the full conductivity tensor σ_{ij} in magnetic field \mathbf{B} , starting from a tight-binding model of the electronic band structure $\epsilon(\mathbf{k})$. The Chambers solution is

$$\sigma_{ij} = \frac{e^2}{4\pi^3} \int d^3\mathbf{k} \left(-\frac{df_0}{d\epsilon} \right) v_i [\mathbf{k}(t=0)] \int_{-\infty}^0 v_j [\mathbf{k}(t)] e^{t/\tau} dt, \quad (2)$$

where $\int d^3\mathbf{k}$ is an integral over the entire Brillouin zone, $\left(-\frac{df_0}{d\epsilon} \right)$ is the derivative with respect to the energy of the equilibrium Fermi distribution function, v_i is the i th component of the quasiparticle velocity and $\int_{-\infty}^0 dt$ is an integral over the lifetime τ of a quasiparticle. The Fermi velocity is calculated from the tight-binding model as $\mathbf{v}_F = \frac{1}{\hbar} \nabla_{\mathbf{k}} \epsilon(\mathbf{k})$. The magnetic field, including its orientation with respect to the crystal axes, enters through the Lorentz force, which acts to evolve the momentum \mathbf{k} of the quasiparticle via $\hbar \frac{d\mathbf{k}}{dt} = e\mathbf{v} \times \mathbf{B}$. Because the magnetic field is explicitly included in this manner, the Chambers solution has the advantage of being exact to all orders in the magnetic field.

The conductivity of a general electronic dispersion $\epsilon(\mathbf{k})$ can be calculated using equation (2)⁵⁹. The factor $\left(-\frac{df_0}{d\epsilon} \right)$ is approximated as a delta function at the Fermi energy in the limit that temperature T is much smaller than any of the hopping parameters in $\epsilon(\mathbf{k})$, as is the case for our experiments. This delta function transforms the integral over the Brillouin zone into an integral over the FS, and introduces a factor of $1/|\nabla_{\mathbf{k}} \epsilon(\mathbf{k})|$, which is the density of states. To numerically perform the integrals in equation (2), the FS is discretized, usually into 10–15 layers along k_z , with 60–100 points per k_z layer; each point is evolved in time using the Lorentz force equation. This moves the quasiparticles along the cyclotron orbits around the FS, and their velocity is recorded at each position and integrated over time. The weighting factor $e^{t/\tau}$ accounts for the scattering of the quasiparticles as they traverse the orbit. In general, τ is taken to be a function of momentum $\tau(\mathbf{k})$, and then the factor $e^{t/\tau}$ is replaced by $e^{\int_0^t dt'/\tau(\mathbf{k}(t'))}$. Equation (2) can be used to calculate any component of the semiclassical conductivity tensor. We use it to calculate ρ_{zz} in Figs. 1–4. Note that because of the highly 2D nature of the FS of Nd-LSCO, we neglect the off-diagonal components of the conductivity tensor and use $\rho_{zz} \approx 1/\sigma_{zz}$.

Nd-LSCO band structure at $p=0.24$. We use a 3D tight-binding model of the FS that accounts for the body-centred tetragonal crystal structure of Nd-LSCO³⁴:

$$\begin{aligned} \epsilon(k_x, k_y, k_z) = & -\mu - 2t[\cos(k_x a) + \cos(k_y a)] \\ & - 4t' \cos(k_x a) \cos(k_y a) - 2t''[\cos(2k_x a) + \cos(2k_y a)] \\ & - 2t_z \cos(k_x a/2) \cos(k_y a/2) \cos(k_z c/2) [\cos(k_x a) - \cos(k_y a)]^2, \end{aligned} \quad (3)$$

where μ is the chemical potential; t, t' and t'' are the first, second and third nearest-neighbour hopping parameters, respectively; t_z is the interlayer hopping parameter; $a = 3.75$ Å is the in-plane lattice constant of Nd-LSCO; and $c/2 = 6.6$ Å is the CuO_2 layer spacing. The interlayer hopping has the form factor $\cos(k_x a/2) \cos(k_y a/2) (\cos(k_x a) - \cos(k_y a))^2$, which accounts for the offset copper oxide planes between the layers of the body-centred tetragonal structure⁶⁰.

The fit results are presented in Fig. 2b (for the ADMR) and Extended Data Table 1 (for the tight-binding and scattering rate parameters). Although the genetic algorithm was allowed to search over a wide range of parameters, we found that the optimal solution converged towards t', t'' and t_z values extremely close to the ARPES values, with a 7% deviation at most for t_z . Only μ , and therefore p , is substantially different from the ARPES value. The higher doping found by ARPES may be due to the difficulty in accounting for k_z dispersion or may be due to different doping levels at the surface. Nevertheless, the shape of the FS found by fitting the ADMR data (Fig. 2b,c) is electron like and qualitatively identical to the one measured by ARPES²², and the doping found by us ($p=0.248$) is very close to the nominal value, namely, $p=0.240 \pm 0.005$ (ref. 7).

This demonstrates that the FS is correctly mapped out by our analysis of the ADMR data. In the figures and analysis presented in this manuscript, we use the tight-binding values from Extended Data Table 1; for simplicity, we refer to them as the ‘tight-binding values from ARPES’, as they only differ by the chemical potential value.

Nd-LSCO scattering rate model at $p=0.24$. We have used a minimal, phenomenological, anisotropic scattering rate model to fit the ADMR data of Nd-LSCO at $p=0.24$, which we refer to as the ‘cosine’ model:

$$1/\tau(T, \phi) = 1/\tau_{\text{iso}}(T) + 1/\tau_{\text{aniso}}(T) |\cos(2\phi)|^\nu, \quad (4)$$

where $1/\tau_{\text{iso}}$ is the amplitude of the isotropic scattering rate, $1/\tau_{\text{aniso}}$ is the amplitude of the ϕ -dependent scattering rate and ν is an integer. The best fit using this model is plotted in Fig. 2b. The features at $\theta=40^\circ$ and $\theta=90^\circ$ are present with the same amplitudes as the data. With as few parameters as possible, this model captures the trend of the anti-nodal regions of the FS to have shorter quasiparticle lifetimes in the cuprates^{61,62}, particularly close to the Van Hove singularity. This model should be seen as the simplest phenomenological model capable of capturing the correct shape of the real scattering rate, with the least number of free parameters. In another study⁸, we explore two other scattering rate models and show that they converge to the same shape as a function of ϕ .

Nd-LSCO large hole-like FS at $p=0.21$. First, we examine the simplest scenario to fit the ADMR at $p=0.21$, which is to keep the tight-binding values from the fit to $p=0.24$ and just shift the chemical potential across the Van Hove singularity to $p=0.21$. We then explore three different types of scattering model: an isotropic scattering rate, the anisotropic ‘cosine’ function from equation (4) and a model of ‘Fermi arcs’. For the Fermi arcs model, the scattering rate is set to a constant value inside the (π, π) -reduced Brillouin zone and set to a different, higher value outside this zone.

The best-fit results for these three models are shown in Extended Data Figs. 2b,c and 3d. All of them fail to capture the correct ϕ dependence of the ADMR around the $\theta=90^\circ$ feature. We conclude that the FS transformation through p^* is not the unreconstructed, hole-like FS.

Nd-LSCO (π, π) FS reconstruction at $p=0.21$. Several different reconstruction scenarios^{19,41–43,45} produce an FS that is qualitatively equivalent to the one produced by a (π, π) antiferromagnetic order parameter⁴³. We simulate such a reconstruction by starting with the tight-binding model at ADMR values for Nd-LSCO at $p=0.24$ (Extended Data Table 1) and performing a 2D (π, π) reconstruction, maintaining the same interlayer coupling terms used in the unreconstructed case. The tight-binding model is then

$$\begin{aligned} \epsilon_{(\pi, \pi)}(k_x, k_y, k_z) = & -\mu + \frac{1}{2} [\epsilon_0(k_x, k_y, k_z) + \epsilon_0(k_x + \pi/a, k_y + \pi/a, k_z)] \\ & - \frac{1}{2} \sqrt{4\Delta^2 + [\epsilon_0(k_x, k_y, k_z) - \epsilon_0(k_x + \pi/a, k_y + \pi/a, k_z)]^2} \\ & - 2t_z \cos(k_z c/2) \cos(k_x a/2) \cos(k_y a/2) [\cos(k_x a) - \cos(k_y a)]^2, \end{aligned} \quad (5)$$

where the unreconstructed ϵ_0 is given by

$$\begin{aligned} \epsilon_0(k_x, k_y, k_z) = & -2t[\cos(k_x a) + \cos(k_y a)] - 4t' \cos(k_x a) \cos(k_y a) \\ & - 2t''[\cos(2k_x a) + \cos(2k_y a)]. \end{aligned} \quad (6)$$

Here Δ is the gap size; t, t' and t'' are the first, second and third nearest-neighbour hopping parameters, respectively; μ is the chemical potential; and t_z is the interlayer hopping parameter.

Note that the above equations consist of a 2D antiferromagnetic model with added interplane hopping instead of a fully 3D antiferromagnetic model. The reason for this is Nd-LSCO’s tetragonal crystal structure, for which the full 3D reconstruction would induce C_4 rotation symmetry breaking (coming

from the $\cos(k_x a/2)\cos(k_y a/2)$ term in interplane hopping). By performing the 2D reconstruction alone, rotational symmetry in the copper oxide planes is preserved. Moreover, such a reconstruction is likely to be more consistent with the short-length spin correlations that are incoherent between planes. Note also that short-range antiferromagnetic correlations could induce a reconstruction as long as the thermal de Broglie wavelength of the electron (of the order of a few nanometres at 6 K given the effective mass at $p=0.21$ (ref. 21)) is shorter than the antiferromagnetic correlation length⁶³.

The ADMR was simulated using equation (5) using a procedure similar to that described above for $p=0.24$. It was found that an isotropic scattering rate allows to optimally fit the data. Thus, the scattering rate, gap magnitude and chemical potential were the only three parameters allowed to vary using the genetic algorithm. The best fit is presented in Fig. 4f, and the fit values can be found in Extended Data Table 2.

To understand the influence of the different parameters on the fit, Extended Data Fig. 7 shows how the ADMR varies with an increasing gap size. Although the magnitude of the overall drop at $\theta=90^\circ$ increases with increasing Δ , the variation is rather slow and no strong qualitative change in the simulations is observed. The best-fit value is found to be around $\Delta=55$ K. We show the same but as a function of the scattering rate amplitude (Extended Data Fig. 8).

The reduction in scattering rate anisotropy when moving from the unreconstructed FS at $p=0.24$ to the nodal hole pockets at $p=0.21$ may be due to the large reduction in anisotropy of the density of states. Extended Data Fig. 5 plots the magnitude of the Fermi velocity—inversely proportional to the density of states—for both unreconstructed FS and nodal hole pockets. Here v_F varies by a factor of 25 for the unreconstructed FS, which is probably the origin of the anisotropic elastic scattering rate. At $p=0.21$, however, v_F varies by just over a factor of two—a huge reduction in anisotropy. This may explain why the scattering rate found by us on the nodal hole pockets is roughly isotropic (note that the scattering rate is not exactly proportional to the density of states, as it depends on the form of the scattering matrix elements). Note that although the relative change in resistivity is reproduced by the model, the absolute value is not reproduced: the absolute resistivity at $\theta=0^\circ$ is $\rho_{xx}=35.80$ m Ω cm, whereas the fit produces $\rho_{xx}=12.93$ m Ω cm. The difference between the model and data may be due to the incoherent contributions to transport, which are not captured by the Boltzmann equation.

Nd-LSCO Hall effect at $p=0.21$. A (π, π) reconstruction at $p=0.21$, with the gap value obtained by our best fit to the ADMR data, also produces small, anti-nodal electron pockets. Although a fit can still be obtained with the electron pockets included (as their inclusion only adds more free parameters to the model), we exclude them from the model based on the calculated Hall coefficient. Extended Data Fig. 4 compares the data taken at 30 K on Nd-LSCO at $p=0.21$ (ref. 20) with the Hall coefficient calculated from several models. The nodal hole pockets on their own produce the best agreement with the data.

Nd-LSCO CDW FS reconstruction at $p=0.21$. A biaxial CDW with a period near to three lattice spacings is thought to underlie the reconstructed pocket observed in quantum oscillation experiments^{32,64}. We simulate such a reconstruction by starting with the ARPES tight-binding values for Nd-LSCO at $p=0.24$ and perform a period-three biaxial wavevector reconstruction of the FS. Similar to (π, π) reconstruction, we perform a 2D reconstruction and maintain the same interlayer coupling terms used in the unreconstructed case. This FS reconstruction produces multiple pockets and open sheets, similar to another study³⁷. We calculate the ADMR for only the diamond-shaped FS because this is the only surface that has been reported by quantum oscillations in underdoped cuprates⁶⁵ and because it is the only FS needed to model the ADMR in $\text{YBa}_2\text{Cu}_3\text{O}_{6.6}$ (ref. 33). The inclusion of any other FSs would lead to a value of the normal-state specific heat that is larger than the measured value⁶⁶.

The Hamiltonian used for finding the in-plane FS can be written as follows⁶⁷:

$$H = \sum_{\mathbf{k}} [\epsilon_0(\mathbf{k})c_{\mathbf{k}}^\dagger c_{\mathbf{k}} - \sum_{\mathbf{Q}} \Delta_{\mathbf{Q}}(\mathbf{k} + \mathbf{Q}/2)c_{\mathbf{k}+\mathbf{Q}}^\dagger c_{\mathbf{k}}], \quad (7)$$

where the sum over \mathbf{k} extends over the entire Brillouin zone of the square lattice, $\Delta_{\mathbf{Q}}$ is the gap of the CDW and \mathbf{Q} is the wavevector of charge ordering. For a bidirectional CDW with a period of three lattice spacings, the sum over \mathbf{Q} extends over the four values of $(\pm \frac{2\pi}{3}, 0)$ and $(0, \pm \frac{2\pi}{3})$. The in-plane electronic dispersion is the same as the in-plane dispersion ϵ_0 described in equation (6). The FS is found by selecting the eigenvalue of the resulting 9×9 matrix that corresponds to the diamond-shaped FS (Fig. 3e).

We calculate the ADMR using the Chambers formula for this model. The result is shown (Fig. 3) for a number of different CDW strengths, as well as for a d -wave form factor. The simulated ADMR is somewhat reminiscent of the $p=0.24$ data, except that the peak that was found at around $\theta=30^\circ$ for $p=0.24$ has been pushed out to $\theta=60^\circ$. This qualitative similarities arise because both unreconstructed FS and small reconstructed diamonds are similar in shape. The features are pushed to higher θ for the reconstructed case because k_F is smaller. It is clear, however, that CDW reconstruction does not match the ADMR for Nd-LSCO at $p=0.21$.

Data availability

Source data are provided with this paper. Other experimental data presented in this paper are available at <http://wrap.warwick.ac.uk/161600/>. The results of the conductivity simulations are available from the corresponding author upon reasonable request.

Code availability

The code used to compute the conductivity is available from the corresponding author upon reasonable request.

References

- Goddard, P. A. et al. Angle-dependent magnetoresistance of the layered organic superconductor κ -(ET)₂Cu(NCS)₂: simulation and experiment. *Phys. Rev. B* **69**, 174509 (2004).
- Chakravarty, S., Sudbø, A., Anderson, P. W. & Strong, S. Interlayer tunneling and gap anisotropy in high-temperature superconductors. *Science* **261**, 337–340 (1993).
- Abrahams, E. & Varma, C. M. What angle-resolved photoemission experiments tell about the microscopic theory for high-temperature superconductors. *Proc. Natl Acad. Sci. USA* **97**, 5714–5716 (2000).
- Analytis, J. G., Abdel-Jawad, M., Balicas, L., French, M. M. J. & Hussey, N. E. Angle-dependent magnetoresistance measurements in $\text{Tl}_2\text{Ba}_2\text{CuO}_{6.6}$ and the need for anisotropic scattering. *Phys. Rev. B* **76**, 104523 (2007).
- Tremblay, A.-M.S. in *Strongly Correlated Systems* (eds Avella, A. & Mancini, F.) 409–453 (Springer, 2012).
- Sebastian, S. E. et al. Normal-state nodal electronic structure in underdoped high- T_c copper oxides. *Nature* **511**, 61–64 (2014).
- Chan, M. K. et al. Single reconstructed Fermi surface pocket in an underdoped single-layer cuprate superconductor. *Nat. Commun.* **7**, 12244 (2016).
- Riggs, S. C. et al. Heat capacity through the magnetic-field-induced resistive transition in an underdoped high-temperature superconductor. *Nat. Phys.* **7**, 332–335 (2011).
- Sachdev, S. & La Placa, R. Bond order in two-dimensional metals with antiferromagnetic exchange interactions. *Phys. Rev. Lett.* **111**, 027202 (2013).

Acknowledgements

We acknowledge helpful discussions with J. Analytis, D. Chowdhury, N. Doiron-Leyraud, N. Hussey, M. Kartsovnik, S. Kivelson, D.-H. Lee, S. Lewin, A.-M. Tremblay, K. Modic, S. Musser, C. Proust and S. Todadri. A part of this work was performed at the National High Magnetic Field Laboratory, which is supported by the National Science Foundation (NSF) cooperative agreement no. DMR-1644779 and the State of Florida. P.A.G. acknowledges that this project is supported by the European Research Council (ERC) under the European Union's Horizon 2020 research and innovation programme (grant agreement no. 681260). J.Z. was supported by an NSF grant (MRSEC DMR-1720595). L.T. acknowledges support from the Canadian Institute for Advanced Research (CIFAR) as a Fellow and funding from the Natural Sciences and Engineering Research Council of Canada (NSERC; PIN: 123817), the Fonds de recherche du Québec—Nature et Technologies (FRQNT), the Canada Foundation for Innovation (CFI), and a Canada Research Chair. This research was undertaken thanks in part to funding from the Canada First Research Excellence Fund. Part of this work was funded by the Gordon and Betty Moore Foundation's EPIQS Initiative (grant GBMF5306 to L.T.), B.J.R. and Y.F. acknowledge funding from the NSF under grant no. DMR-1752784.

Author contributions

A.L., P.A.G., L.T. and B.J.R. conceived the experiment. J.Z. grew the samples. A.L., F.L., A.A., C.C. and M.D. performed the sample preparation and characterization. Y.F., G.G., A.L., D.G., P.A.G. and B.J.R. performed the high-magnetic-field measurements at the National High Magnetic Field Laboratory. Y.F., G.G., S.V., M.J.L. and B.J.R. performed the data analysis and simulations. Y.F., G.G., S.V., P.A.G., L.T. and B.J.R. wrote the manuscript with input from all the other co-authors. L.T. and B.J.R. supervised the project.

Competing interests

The authors declare no competing interests.

Additional information

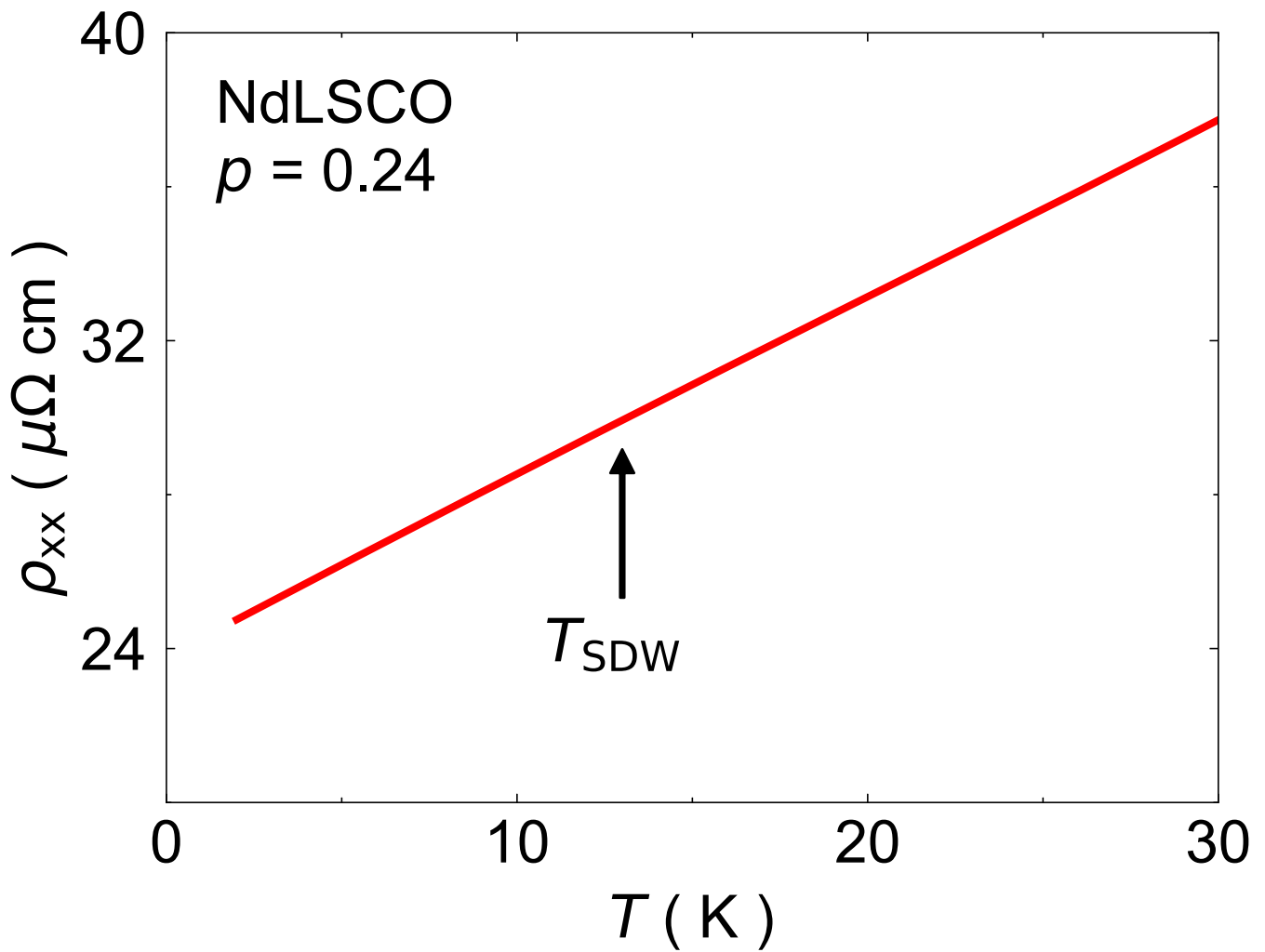
Extended data is available for this paper at <https://doi.org/10.1038/s41567-022-01514-1>.

Supplementary information The online version contains supplementary material available at <https://doi.org/10.1038/s41567-022-01514-1>.

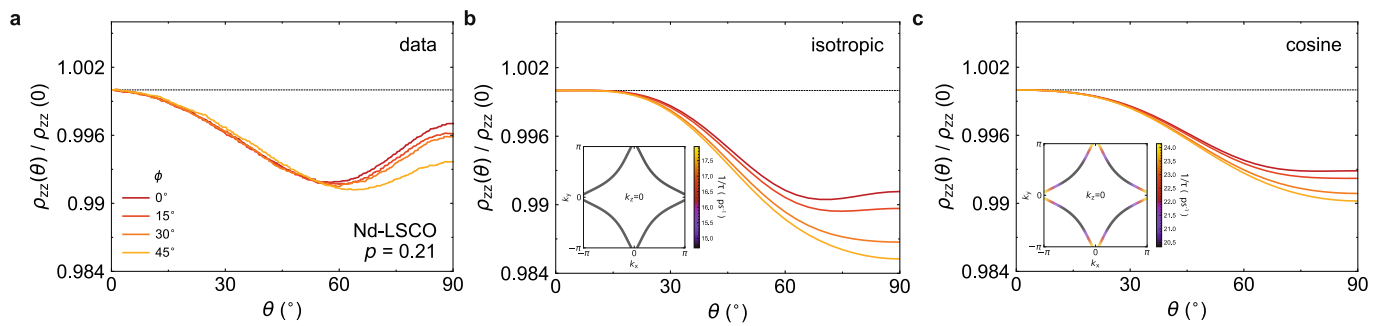
Correspondence and requests for materials should be addressed to B. J. Ramshaw.

Peer review information *Nature Physics* thanks the anonymous reviewers for their contribution to the peer review of this work.

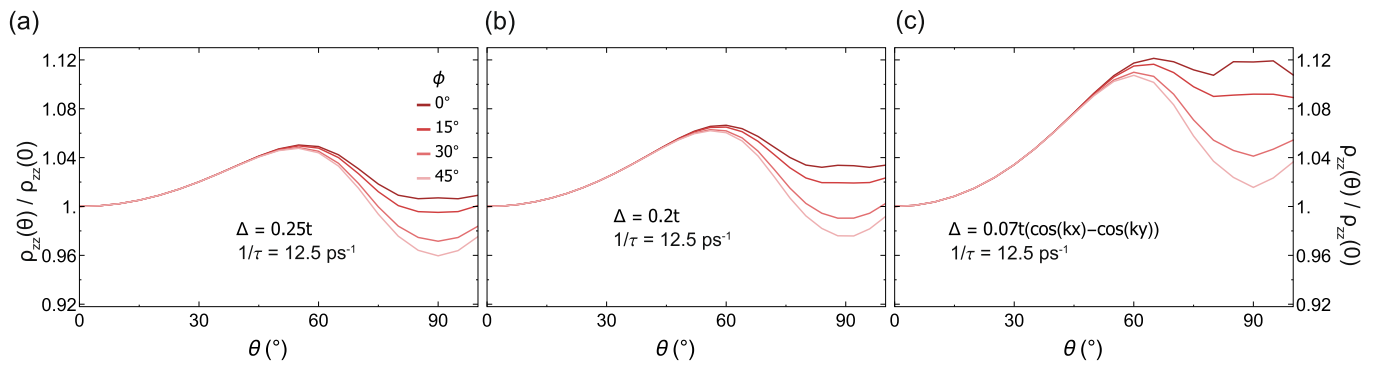
Reprints and permissions information is available at www.nature.com/reprints.



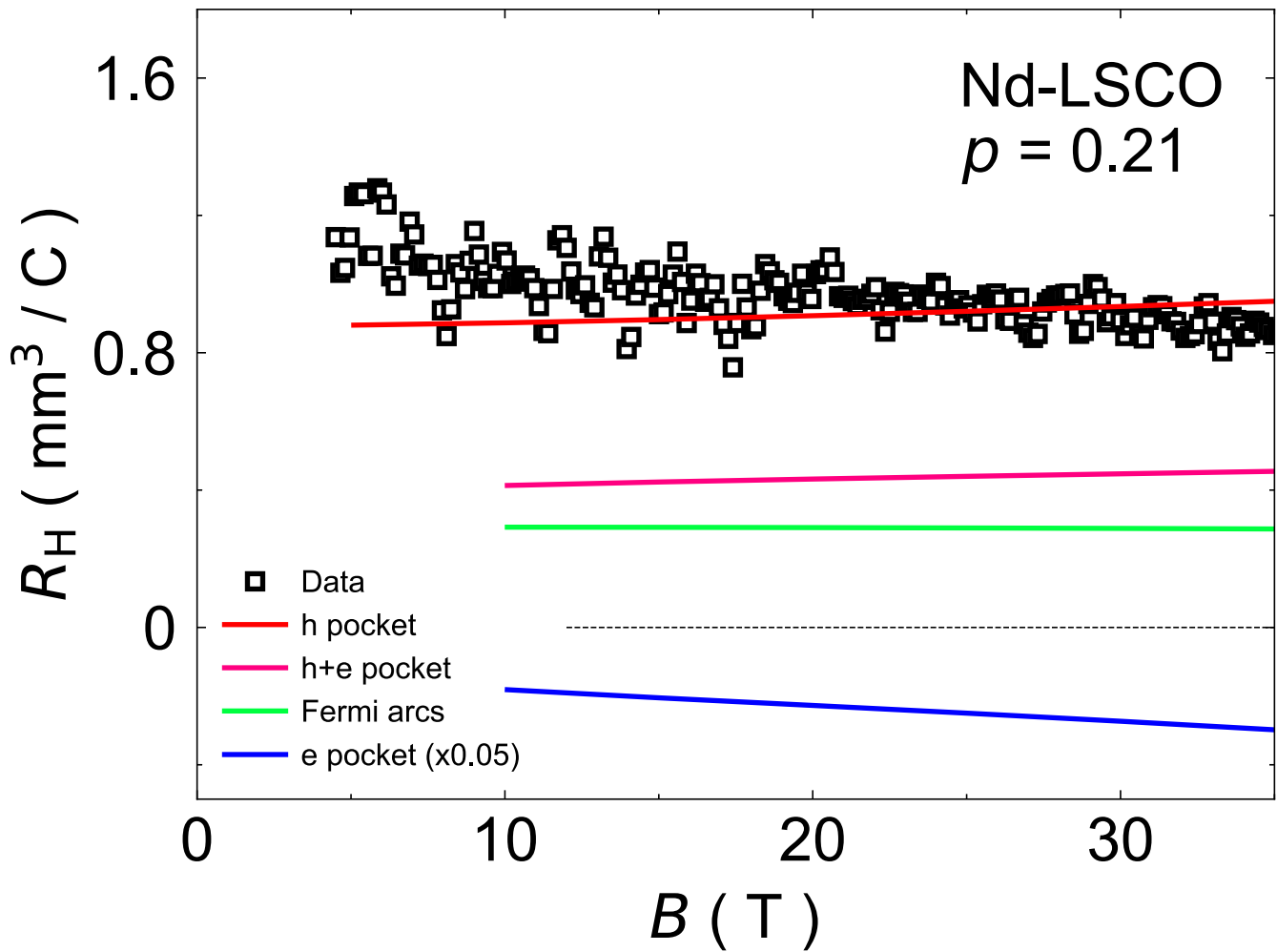
Extended Data Fig. 1 | Resistivity of Nd-LSCO at $p = 0.24$ near T_{SDW} . In-plane resistivity data at $B = 35$ T as a function of temperature (reproduced from ref.²⁰). The resistivity ρ_{xx} (red line) is perfectly linear over this temperature range without any sign of an upturn or even a change in slope at $T_{SDW} = 13 \pm 1$ K (black arrow) reported by Ma et al.¹⁵ at $B = 0$ T. This suggests that either the SDW is not present in our samples or that the SDW vanishes in a magnetic field and thus does not interfere with our measurements performed at $B = 45$ T.



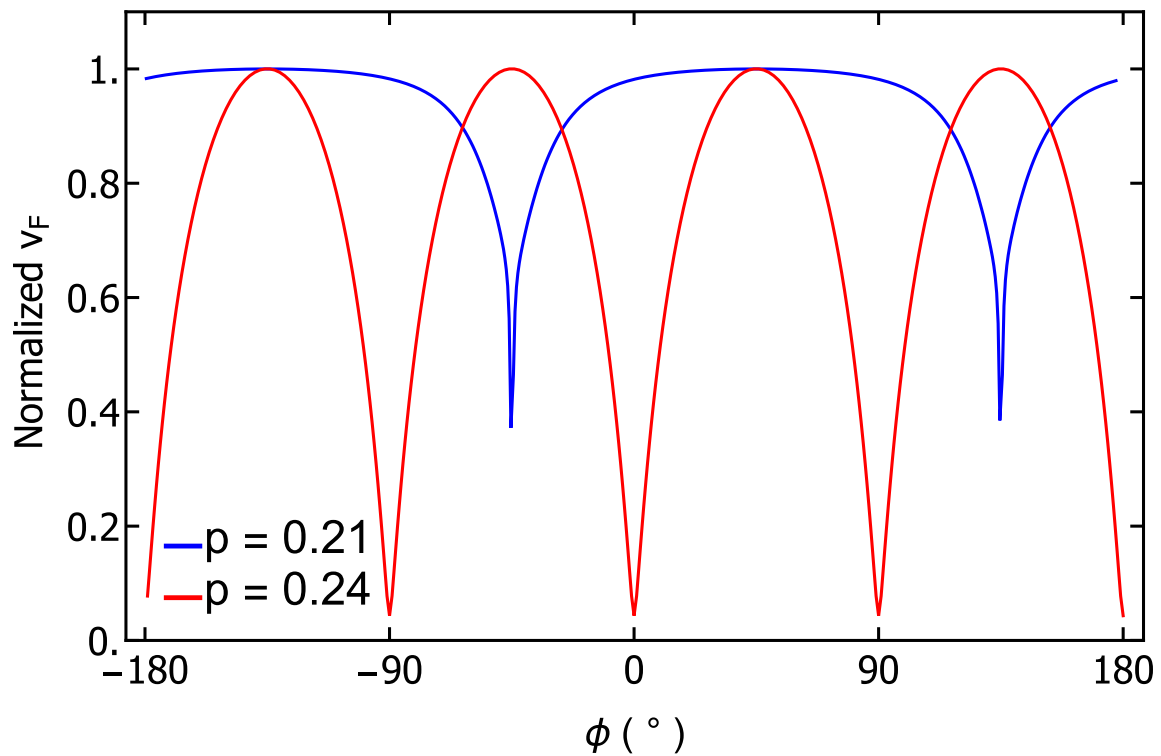
Extended Data Fig. 2 | Best fit of Nd-LSCO $p = 0.21$ data with the large, hole-like, unreconstructed Fermi surface. (a) ADMR data on Nd-LSCO $p = 0.21$ at $T = 25$ K and $B = 45$ T; (b, c) The best fits for the ADMR data in (a) using the band structure ARPES values for Nd-LSCO $p = 0.24$ with the chemical potential shifted across the van Hove point (at $p \approx 0.23$) to $p = 0.21$, where the Fermi surface is hole-like. Insets represent the scattering rate distribution values over the hole-like Fermi surface at $p = 0.21$. In (b), the scattering is isotropic over the Fermi surface; in (c) we use the cosine scattering rate model (this figure differs from Fig. 3b because there we only shift the chemical potential, while here we show the best-fit using this model).



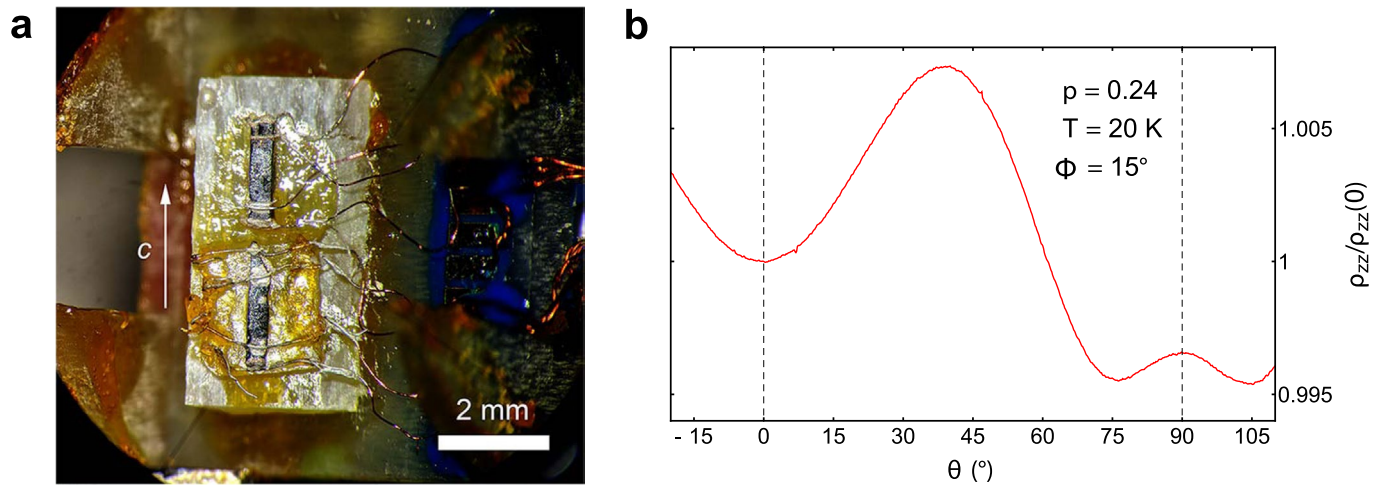
Extended Data Fig. 3 | Calculation of ADMR for a period three CDW Fermi surface reconstruction. Calculations using two different gap sizes are shown in (a) and (b), and using a d -wave form factor is shown in (c).



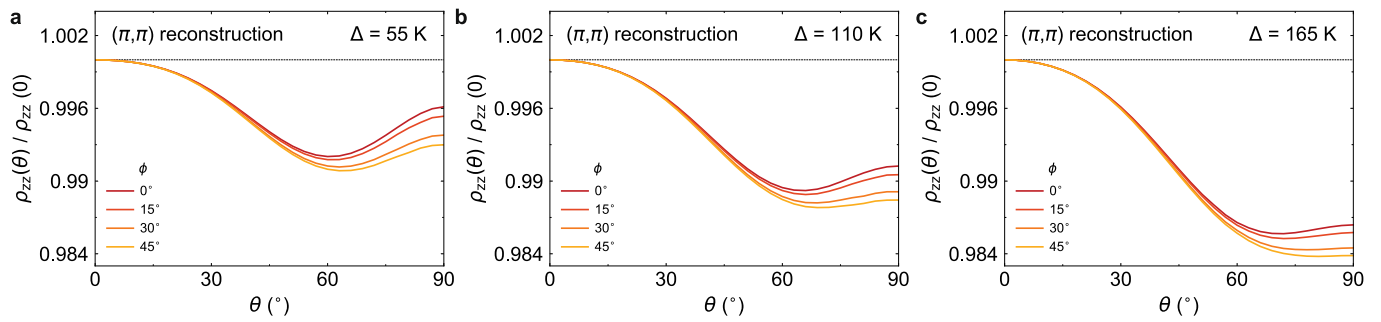
Extended Data Fig. 4 | The Hall effect in Nd-LSCO at $p = 0.21$. The data is taken at 30 K and is reproduced from Collignon et al.²⁰. 'h pocket' is from the fit to the data shown in Fig. 4 of the main text; 'h+e pocket' is from a fit that includes both the hole and electron pockets after (π, π) reconstruction; 'Fermi arcs' is from the fit in Fig. 3c,d of the main text; 'e pocket' is from just the electron pocket produced by (π, π) reconstruction, scaled down by a factor of 20 for clarity.



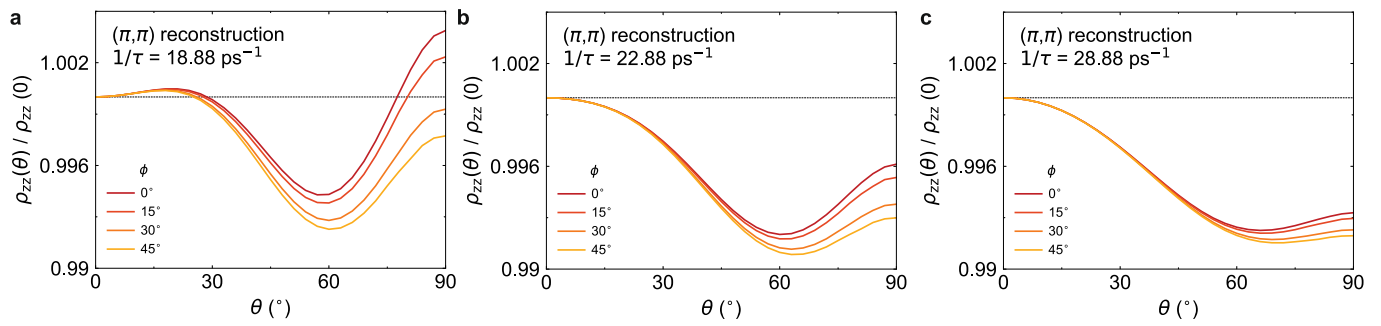
Extended Data Fig. 5 | Variation in the Fermi velocity around the Fermi surface above and below p^* . The red curve plots the magnitude of the Fermi velocity around the Fermi surface at $p = 0.24$, as shown in Fig. 2. The blue curve plots the same quantity for a single nodal hole pocket, as shown in Fig. 4 (the reduction in symmetry is because each nodal hole pocket is 2-fold symmetric). The total anisotropy in v_F around the Fermi surface is a factor of 25 at $p = 0.24$, but just larger than a factor of 2 at $p = 0.21$.



Extended Data Fig. 6 | ADMR experimental set up. (a) An illustration of the sample mounting. The two samples here are mounted on a G-10 wedge to provide a ϕ angle of 30° . Additional wedges provided angles of $\phi = 15^\circ$ and 45° ; (b) ADMR as a function of θ angle from -15° to 110° and $\phi = 0$ at $T = 20 \text{ K}$ for Nd-LSCO $\rho = 0.24$, showing the symmetry of the data about these two angles.



Extended Data Fig. 7 | ADMR dependence on the gap amplitude with (π, π) reconstruction. ADMR calculations with a (π, π) reconstructed Fermi surface for different gap amplitudes at fixed isotropic scattering rate value $1/\tau = 22.88$ ps $^{-1}$. Note that this is within $\approx 40\%$ of the nodal scattering rate at $p = 0.24$, consistent with a nodal hole pockets reconstructed from the larger Fermi surface.



Extended Data Fig. 8 | ADMR dependence on the scattering rate amplitude with (π, π) reconstruction. ADMR calculations with a (π, π) reconstructed Fermi surface for different isotropic scattering rate amplitudes at fixed gap value at $\Delta = 55 \text{ K}$.

Extended Data Table 1 | Tight-binding parameters from the fit to the ADMR data at $p = 0.24$. Best fit tight-binding values for the Nd-LSCO $p = 0.24$ ADMR data (using the cosine scattering rate model of Equation (4)). The results are extremely close to ARPES tight-binding values reported in Matt et al.²² and Horio et al.³⁴, reproduced here on the second line. Error bars on the ADMR-derived hopping parameters and chemical potential are all ± 0.0005 , and were obtained following the procedure described in the above section. The error bar on the value of t_z measured by ARPES is $\pm 0.02t$ (J. Chang and M. Horio, private communication)

	t (meV)	t'	t''	t_z	μ	p	$1/\tau_{\text{iso}}$ (ps^{-1})	$1/\tau_{\text{aniso}}$ (ps^{-1})	ν
ADMR	160 ± 30	$-0.1364t$	$0.0682t$	$0.0651t$	$-0.8243t$	0.248	12.595 ± 0.002	63.823 ± 0.26	12 ± 1
ARPES	190	$-0.136t$	$0.068t$	$0.07t$		0.28			

Extended Data Table 2 | Results of the fit of the Nd-LSCO $p = 0.21$ data with (π, π) reconstruction. Fit parameter values for Nd-LSCO $p = 0.21$ plotted in Fig. 4f. The band structure parameters were kept fixed at ARPES values²². Error bars were obtained following the procedure described in the above section

T (K)	μ	$1/\tau_{\text{iso}}$ (ps^{-1})	Δ (K)
25	$-0.495t \pm 0.01$	22.88 ± 0.30	55 ± 11